

Soil and Vegetation Spectral Coupling Difference (SVSCD) for Minerals Extraction from Hyperion Data in Vegetation Covered Area

CHEN Shengbo¹, HUANG Shuang¹, LIU Yanli¹, ZHOU Chao^{1, 2}

(1. College of Geoexploration Science and Technology, Jilin University, Changchun 130026, China; 2. National Marine Environmental Monitoring Center, Dalian 116023, China)

Abstract: Remote sensing data have been widely applied to extract minerals in geologic exploration, however, in areas covered by vegetation, extracted mineral information has mostly been small targets bearing little information. In this paper, we present a new method for mineral extraction aimed at solving the difficulty of mineral identification in vegetation covered areas. The method selected six sets of spectral difference coupling between soil and plant (SVSCD). These sets have the same vegetation spectra reflectance and a maximum different reflectance of soil and mineral spectra from Hyperion image based on spectral reflectance characteristics of measured spectra. The central wavelengths of the six, selected band pairs were 2314 and 701 nm, 1699 and 721 nm, 1336 and 742 nm, 2203 and 681 nm, 2183 and 671 nm, and 2072 and 548 nm. Each data set's reflectance was used to calculate the difference value. After band difference calculation, vegetation information was suppressed and mineral abnormal information was enhanced compared to the scatter plot of original band. Six spectral difference couplings, after vegetation inhibition, were arranged in a new data set that requires two components that have the largest eigenvalue difference from principal component analysis (PCA). The spatial geometric structure features of PC1 and PC2 was used to identify altered minerals by spectral feature fitting (SFF). The collecting rocks from the 10 points that were selected in the concentration of mineral extraction were analyzed under a high-resolution microscope to identify metal minerals and nonmetallic minerals. Results indicated that the extracted minerals were well matched with the verified samples, especially with the sample 2, 4, 5 and 8. It demonstrated that the method can effectively detect altered minerals in vegetation covered area in Hyperion image.

Keywords: spectral difference coupling; vegetation covered area; Hyperion image; mineral extraction

Citation: CHEN Shengbo, HUANG Shuang, LIU Yanli, ZHOU Chao, 2018. Soil and Vegetation Spectral Coupling Difference (SVSCD) for Minerals Extraction from Hyperion Data in Vegetation Covered Area. *Chinese Geographical Science*, 28(6): 957–972. <https://doi.org/10.1007/s11769-018-1005-z>

1 Introduction

Remote sensing imagery of mineral characteristics has been widely applied to investigate geological landforms in arid, semi-arid and vegetation covered areas. For instance, hydrothermal alteration zoning can be mapped using clay minerals and individual iron using the spe-

cific absorption features of the minerals found on hyper-spectral images (Sabins, 1999). In the mineral spectra, the position of the diagnostic absorption features was largely determined by electron-transition following ions of transition metals like Fe, Ti, Cr and vibrational courses in hydroxyl and H₂O (Hunt, 1977; Pour et al., 2013). As a result, hydrothermal alteration minerals can

Received date: 2018-05-07; accepted date: 2018-09-02

Foundation item: Under the auspices of National Science and Technology Major Project of China (No. 04-Y20A35-9001-15/17), the Program for JLU Science and Technology Innovative Research Team (No. JLUSTIRT, 2017TD-26), the Changbai Mountain Scholars Program, Jilin Province, China

Corresponding author: CHEN Shengbo. E-mail: chensb0408@126.com

© Science Press, Northeast Institute of Geography and Agroecology, CAS and Springer-Verlag GmbH Germany, part of Springer Nature 2018

be identified with absorption features (Clark, 1999; van der Meer, 2004), especially in arid and semi-arid areas. Spectral information from soil and rock is particularly useful as it can be imaged directly from large exposures of geologic materials (El Desouky et al., 2008; Massironi et al., 2008; Pour and Hashim, 2011; 2013; Rajendran et al., 2012).

Alteration mineral signatures can be extracted using mineral absorption characteristics in arid and semi-arid regions. Sabins (1999) applied a spectral unmixing program to process images showing spectral end-member abundances of alteration minerals with Airborne Visible Infrared Imaging Spectrometer (AVIRIS) images. They successfully extracted illite, alunite and kaolinite. Absorption at 2200 nm due to Al-hydroxyl, reveals the presence of clay minerals and sericite, whereas absorption at 2260 nm is due to Fe-hydroxyl (Di Tommaso and Rubinstein, 2007). Gabr et al. (2010) developed a mineral extraction method based on images with divergent band ratios (4/8, 4/2, and 8/9 in RGB) and n -dimensional spectral feature space. Their results indicated that this was a useful tool for identifying auriferous alteration zones and showing promise for alteration zones exploration in similar areas elsewhere. Pour and Hashim (2011; 2012a; 2012b; 2013) selected copper mining districts by PCA, minimum noise fraction transformation (MNF) and band ratio from Advanced Spaceborne Thermal Emission and Reflection Radiometer (ASTER) data. Based on distinctive shortwave infrared (SWIR) properties of the ASTER data, these techniques discriminated hydrothermal alteration mineral zones related to porphyry copper mineralization at a regional scale and predicted of porphyry copper mineralization. Results indicated that the integration of image processing techniques has the ability to reveal significant information for porphyry copper exploration at a regional scale. Vaughan et al. (2003) generated mineral maps using automatic pixel classifications and found key mineral components of geologic units in Spatially Enhanced Broadband Array Spectrograph System (SEBASS) hyperspectral thermal infrared images. Sillitoe and Hedenquist (2003) showed that alunite has unique spectral features that can be associated with high sulphidation epithermal gold. Mapping of hydrothermal alteration minerals, such as kaolinite, pyrophyllite and alunite, from hyperspectral data resulted in an improved understanding of alteration patterns of geological units (Mi-

kucki and Ridley, 1993).

However, in vegetation covered areas, the application of remote sensing for mineral extraction has been much more limited (Carranza and Hale, 2002; Galvão et al., 2005; Blouin et al., 2009; Vicente and de Souza Filho, 2011; Yang et al., 2017). Two band ratio images of Landsat Thematic Mapper (TM) were generated to map, using PCA, hydrothermal alteration zones in heavily vegetated covered areas based on published reflectance spectra (Carranza and Hale, 2002). Based on the diagnostic spectral features of altered minerals, SWIR bands of ASTER data have been used to identify the spectral discrimination of hydrothermally altered materials. The classification angles of spectral angle mapper (SAM) for identification of hydroxyl-bearing minerals were a slight improvement due to the presence of sparse grass cover in the alteration zone. As a result, the extraction of hydroxyl-bearing minerals using ASTER images was limited to a small number of pixels from exposed areas (Galvão et al., 2005). Based on the multiple linear regression method of composite spectral mixtures, including quartz, aluminum hydroxyl minerals and vegetation, a genetic programming was applied to mineral classification in areas of dense vegetation. Surface vegetation vaporization can be offset by the vegetation corrected continuum depth (VCCD) method when 2200 nm continuum removed band depth (CRBD) was found (Blouin et al., 2009). ASTER images and reflectance spectra were used to detect mineral components of soils covered with vegetation in Brazil indicating the possibility to distinguish between iron-rich and iron-poor soils (Vicente and de Souza Filho, 2011). The extraction and remote mapping of minerals such as montmorillonite, gibbsite and kaolinite was also shown to be feasible (Vicente and de Souza Filho, 2011).

The hyperspectral sensor data product is a 'cube' of data or a three-dimensional array, in which the length and width is correspond to spatial dimensions while the spectrum of every point is in the third dimension (Landgrebe, 2002). This provides the possible benefit of collecting more detailed information than previously (Pour and Hashim, 2014) with the corollary that high dimensional hyperspectral data could challenge current data processing methods (Pour et al., 2014).

The earth surface is a consistent set of characteristic ground materials with relatively stable spectra, including grass, soil, water and shadow. The occurrence, loca-

tion and characteristics of a certain percentage of these members causes most spectral changes of surface scenes (Ju et al., 2003). The spatial geometric-structure features of alteration information, background and interference in characteristic space was investigated by the analysis of two-dimensional and three-dimensional scatter diagrams based on the statistical features of remote sensing data. The results demonstrated that the anomalous point groups, including alteration information, usually dissociated out of the hyperplane (Yang et al., 2009). Zhang et al. (2010) analyzed the spatial geometric-structure features of the two-dimensional scatter plots generated by different histograms and the positioning in abnormal information space. They demonstrated the importance and practicality of spatial structure analysis using remote sensing data in altered mineral information extraction (Zhang et al., 2010; Hu et al., 2011).

Reflectance spectroscopy is an alternative technique that used spectral absorption features between visible/near infrared (VNIR) and SWIR wavelengths (300–2500 nm) for determining mineralogy. A common method is to map mineral formations using remotely sensed spectral reflectance, particularly in arid and semi-arid landscapes. But where vegetation covers areas, these methods can not be effectively applied because of the lack of exposed bedrock, prompting a desire for new algorithms to map rock types and extract minerals using soil and vegetation spectra in vegetation covered areas. In this paper, spectral difference coupling between soil and plant (SVSCD) was applied to mineral extraction from Hyperion images in a vegetation covered area. The difference between soil and vegetation was used for suppressing vegetation information. The extracted minerals matched well with field verification points and demonstrated that the method can effectively extract altered minerals in vegetation covered areas.

2 Geological Setting

The study area is located in Huma, at the northwest corner of Heilongjiang Province, China (50°51′–51°40′N, 126°06′–126°55′E). This is the northern edge of the temperate zone with a cold-temperate, continental monsoon climate. The soil is dominated by both dark-brown forest and brown-coniferous forest soils with minor components of bog and meadow soils. Forest vegetation is typical of cold belt, temperate conifer-

ous. Vegetation coverage of study area is more than 95%; a mix of grasslands, shrubs and trees (Fig. 1). Vegetation species mainly included *Betula platyphylla*, *Carex rigescens*, *Lespedeza bicolor*, *Pinus koraiensis*, *Quercus mongolica* and *Larix gmelinii* without obvious zonal characteristics.

The study area is tectonically dominated by two fractures (northeast and northwest) and folds that play an important role in the formation and distribution of metallic minerals and magmatic activities. The northeast folded belt belongs to the early folding system of Variscian under the influence of early Variscian orogeny. The terrain is also controlled by lithology with granites strongly spheroidally weathered and mountain slopes long and gentle. Mountains in the area consist of high and steep volcanic cones. The study area mainly consists of Ordovician, Silurian, and Devonian layers. They are composed of volcanic-flysch formations of the Tongshan Group and volcanic-sedimentary rocks formation of the Duobaoshan Group and accumulate rich ore-forming materials (Wei et al., 2011). Volcanic rocks composed of marine terrigenous clastic rocks were formed during the Silurian System. In the lower Cretaceous period, the Guanghua Group consisted of gray-green rhyolitic tuff, acid pyroclastic rocks and rhyolite, which was in parallel, unconformable contact with

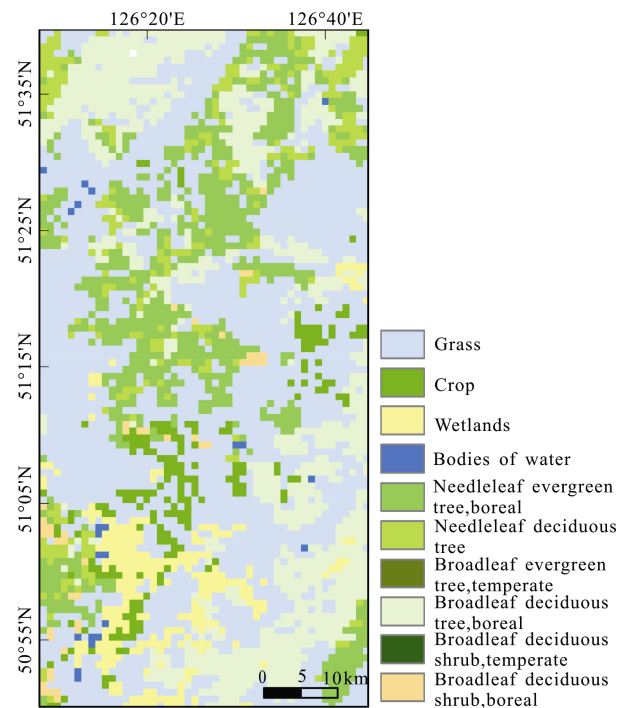


Fig. 1 The vegetation cover map of study area

the Longjiang Group with unclear boundary. The Longjiang Group of lower Cretaceous consisted of gray-black andesite and andesitic tuff. Gray-black basalt, stomatal basalt, tuff and sandy mudstone composed Ganhe Group in the lower Cretaceous. The Quaternary Holocene consisted primarily of depositional sand, sand gravel, sandy clay and silt. Principally defining the shape of the intrusive rocks are batholiths and stocks, followed by small rock bodies in veins. The major rock types are intermediate-plutonic intrusive rocks, consisting of monzogranites, granodiorites, plagiogranites, alaskite-granites and peridotites in upper Permian (Wei et al., 2011). Granodiorites were closely related to ore-formation. Acidic, volcanic rocks consisted of rhyolite, dacite and tuffolava in the Longjiang Group, while intermediate basic volcanic rocks were composed of basalt, andesitic

porphyrite, and tuffolava in the Ganhe Group, Variscan granite, as well as Yanshan granites. Sedimentary rocks with small distribution area are exposed widely in study area (Fig. 2). Commercial mineral resources are found in the important metallogenic belt, Sankuanggou-Duobaoshan tectonic magmatic active belt, including, among others, copper, gold, molybdenum and iron. They form many deposits with high production value including large porphyry Duobaoshan copper and molybdenum deposits, small skarn type Sankuanggou copper and iron deposits, and medium-sized zhengguang gold deposits. Regional mineral resources are equally-spaced, zoned, multiphased and multistaged. The hydrothermal alteration of resources is the result of tectonism and magmatism from the Variscan to the Yanshan periods.

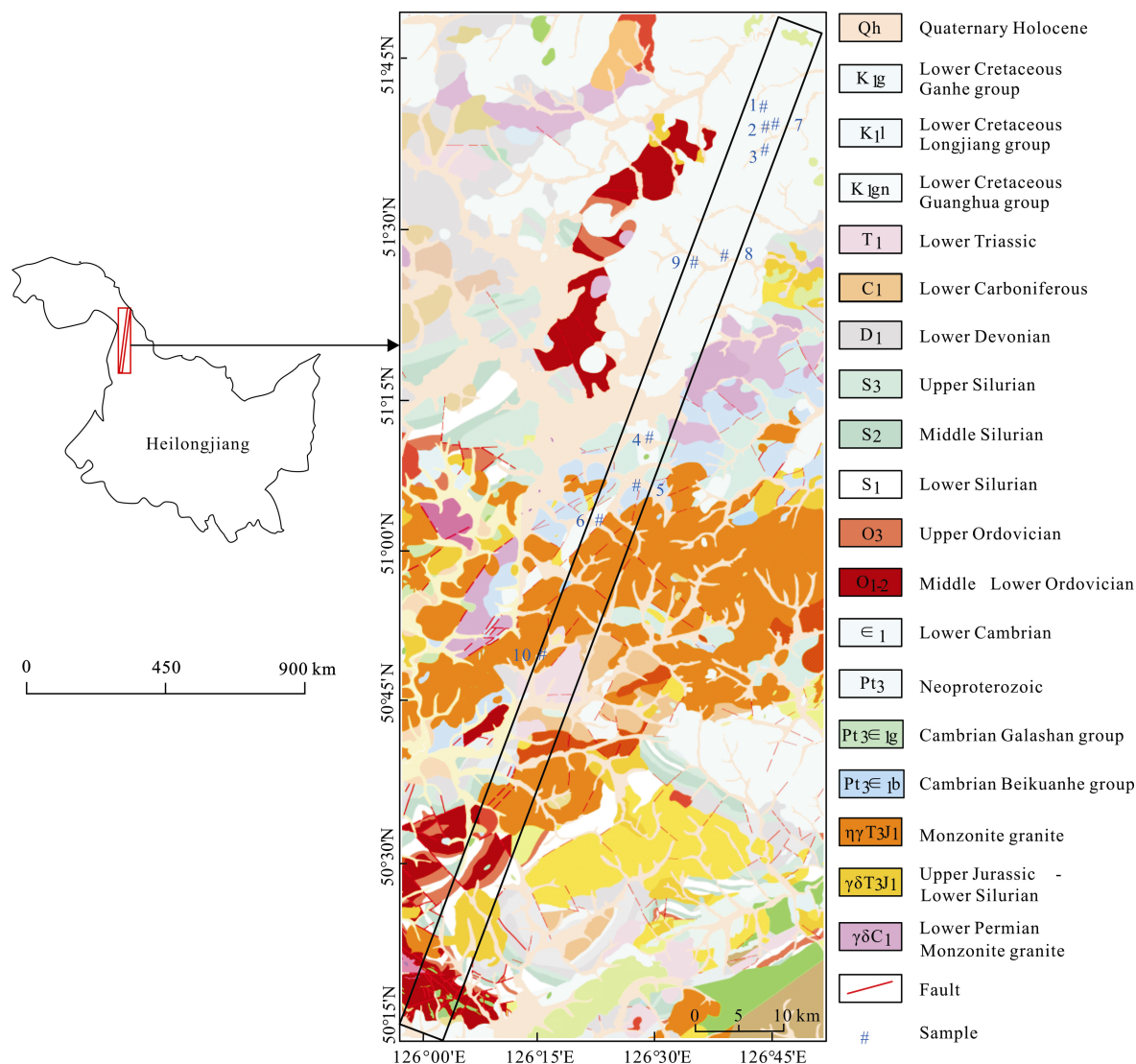


Fig. 2 The geological map of study area

3 Data

3.1 Hyperion Image

For nearly two decades, most of the information on the composition of surface materials has been provided by airborne hyper-spectral sensors. Based on the success of the Hyperion platform, the first spaceborne imaging spectrometer aboard Earth Observing 1 (EO-1) satellite, important milestones in remote sensing research have been achieved. Hyperion covers the spectral range from 400–2500 nm with 30 m spatial resolution, 242 spectral bands and about 10 nm of spectral resolution from a 705 km high orbit. Hyperion scenes are a narrow strip of about 7.7 km of the earth's surface across-track, 42 km or 185 km on the along-track direction. The Hyperion system had two grating spectrometers; a VNIR spectrometer (400–1000 nm) and a SWIR spectrometer (900–2500 nm).

The study area image was acquired by the EO-1 in September 2001 and was L1B-level data. Preprocessing was needed to convert radiance into spectral reflectance of terrestrial materials and reduce sensor error influence. Before atmospheric correction, un-calibrated and water-affected bands were removed. Then the remaining 176 bands were converted into absolute radiance values. Bad lines due to sensor calibration errors were repaired after calibration. Atmospheric correction was done with water vapor content, the aerosol model, atmospheric model and other parameters (see below). The resulting radiance data were converted into surface spectral reflectance for the identification of altered minerals.

3.2 Spectral Measurements

Rock outcropping composition, vegetation species, rock, soil, and vegetation samples were collected over a wide range of study area using local information. Rock and soil samples were collected from non-vegetated areas and rock outcrops as were the spectral characteristics of the ground-measured. On satellite image, the rock sample was covered by the upper canopy. In order to analyze how to obtain the rock and mineral information under vegetation cover on the image, the characteristics of the ground measured spectra were analyzed.

Simultaneous spectral reflectance of these samples was also measured locally. Soil samples were collected at 10–20 cm, 20–30 cm and 30–40 cm depths from the ground surface. Mixed soil samples from different

depths were used to represent average soil conditions in the study area. Leaves of five plant species that were ecologically dominant were collected (*Betula platyphylla*, *Carex rigescens*, *Lespedeza bicolor*, *Pinus koraiensis*, *Quercus mongolica* and *Larix gmelinii*). Spectral reflectance was measured using an ASD Field-Spec Pro field portable spectrometer with the spectral range of 350–2500 nm. Spectral resolution was 3 nm in the 350–1000 nm range and 10 nm at 1000–2500 nm. To ensure the uniformity and effectiveness of spectral curves, all spectra were measured in cloudless conditions from 1000–1400 h. For each sample, 10 spectra were collected and pooled, with their average used as the sample reflectance spectrum. Sample type, test time, longitude and latitude were recorded in detail for each measurement. Due to instrument instability, variation in illumination conditions, atmospheric water vapor interference, large reflectance fluctuations exist in spectral ranges 1350–1420 nm, 1800–1970 nm, and 2308–2500 nm (Fig. 3). To accurately characterize soil and vegetation spectral features, least squares polynomial smoothing was applied to the whole curve.

4 Methods

4.1 Spectral characteristic of soil, minerals and vegetation

The spectrum between 1200 and 2500 nm is usually dominated by the characteristics of a clay mineral (Hubbard et al., 2003), whereas the spectrum with the wavelength range less than 1200 nm is dominated by the characteristics of a few iron-bearing minerals. The absorption band of iron bearing minerals such as goethite and hematite are 500 nm and 900 nm (Hubbard and Crowley, 2005) (Fig. 4A). The absorption bands of Al-OH-containing minerals such as montmorillonite are at the 2170–2210 nm (Crowley et al., 2003). The absorption bands of Mg-OH containing minerals such as chlorite and epidote are at 2315–2335 nm (Fig. 4B). Some of the spectral features of alteration minerals occur near 1400 nm and 1900 nm (Curran et al., 2001) are obscured by atmospheric absorption, so they have no use for conventional remote sensing techniques that use solar energy as the radiation source. Spectra reflection of carbonate minerals after 2000 nm is similar to the clay minerals, but the decreased extent of the reflection between 1800–2000 nm is smaller than clay minerals

(Sabins, 1999). Carbonate minerals spectra near 2300nm and 2450nm has strong absorption because of the CaCO_3 (Fig. 4C).

Soil is a mixture of many substances whose reflec-

tance is influenced by minerals, organics and water dominated by the soil parent materials. Soil parent materials contain hematite, pyrite and trace amounts of carbonate and clay minerals, all of which have an impact

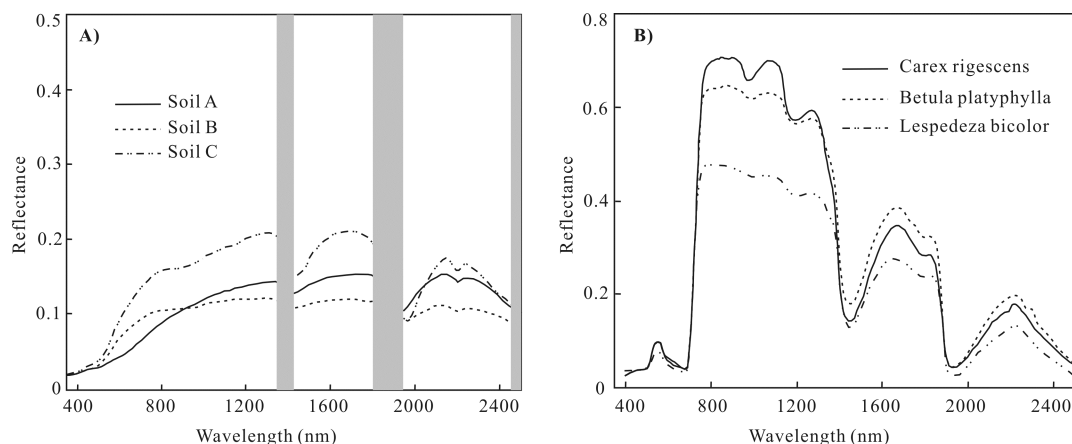


Fig. 3 Soil and vegetation spectra from study area. A) Spectra of soil from three sampling points; B) spectra of *Betula platyphylla*, *Carex rigescens*, and *Lespedeza bicolor*. The gray area in Fig. 3A were the water vapor absorption bands

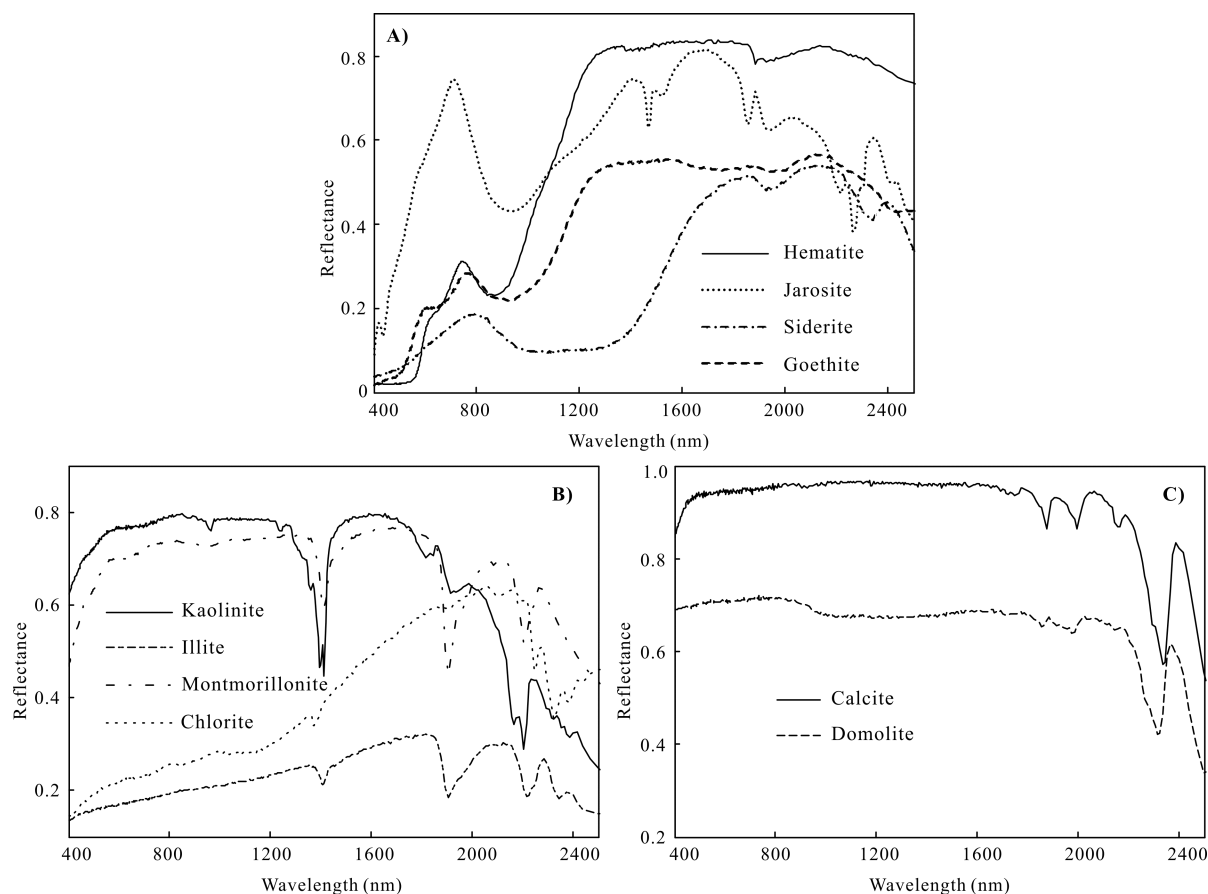


Fig. 4 Spectra of typical minerals from the USGS Mineral Spectral Library. A) Spectra of iron oxide minerals including goethite, siderite, hematite and jarosite, B) spectra of clay minerals including kaolinite, montmorillonite, illite and chlorite, C) spectra of carbonate minerals including calcite and domolite

on radiation spectra (Stoner and Baumgardner, 1981). The spectral reflectance is negatively related to iron content, which enhances the absorption of soil spectra in VNIR bands depending upon the associated environment. All else being equal, spectral reflectance also tends to decrease with an increase of the water content. Organics influence the spectrum between 600–800 nm. Therefore, the spectra of different soil sampling points A, B, C that were randomly selected, are quite different (Fig. 3A).

Characteristics of leaf tissue, structure, plant health and growth phase confer identifiable reflectance patterns. Spectral features at 450 nm and 650 nm are affected by chlorophyll (Gong et al., 2003). Between these two bands, chlorophyll absorption is low with a reflectance peak near 540 nm; a basic characteristic of vegetation in the VNIR bands (Fig. 3B). Lutein and carotene also have absorption at 450 nm, but they are weaker than chlorophyll. Therefore, the spectrum shows chlorophyll absorption features in the healthy vegetation (Sims and Gamon, 2003). In the near-infrared bands, vegetation spectra show high reflectance, high transmittance and low absorption characteristics. Spectral reflectance rises rapidly near 760 nm and forms a distinctive ‘red edge’. The presence of water can be detected at four absorption bands; 960 nm, 1100 nm, 1400 nm and 1900 nm (Fig. 3B).

4.2 The choice of spectral difference coupling

To identify minerals under dense, vegetation cover we proposed a method based on spectral differences between field-measured soil and vegetation that uses their spectral differences calculation to suppress vegetation information. The spectral difference equation is:

$$R = R_{b1} - R_{b2} \quad (1)$$

where R is the reflectance at different bands. $b1$ and $b2$ are bands with the same vegetation reflectance but the difference of soil reflectance is large. This algorithm is more effective (contains more information) when $b1$ and $b2$ are selected for minerals that have a characteristic absorption (e.g., 900 nm for iron-bearing minerals, 2200 nm for hydroxyl minerals and 2350 nm for carbonate minerals; Crowley et al., 2003). The soil, vegetation and mineral spectra collected from the same sampling point were selected for spectral analysis.

Using the vegetation inhibition method, we found six data sets with obvious differences between soil and vegetation reflectance. Based on this, we selected these for vegetation suppression: 2314 and 701 nm, 1699 and 721 nm, 1336 and 742 nm, 2203 and 681 nm, 2183 and 671 nm, and 2072 and 548 nm (Fig. 5). The reflectance of each data set is used to calculate the difference value while the vegetation spectral information is inhibited through the difference calculation, while soil and rock information is highlighted.

4.3 Principal Component Analysis (PCA)

By analyzing eigenvector values, principal components (PCs) that include spectral information of specific minerals can be found. The contribution of the principal components from each original band has a relationship with the spectral response of interested materials (Eklundh and Singh, 1993). Information in data variance is maximized by finding a unique suit of orthogonal axes that originate at and rotate from the data mean. The linear combinations of original spectral bands compose the PC bands that can be calculated as input spectral bands. The first PC band includes the largest percentage of data variance with progressively less data variance explained by subsequent PC bands (Chen and Qian, 2011). In this paper, PCA was applied to all spectral difference coupling bands that were selected to suppress vegetation information. PC1 and PC2 with higher values and opposite signs plotted to get results of anomalous distributions, because they contained more mineral information (Table 1).

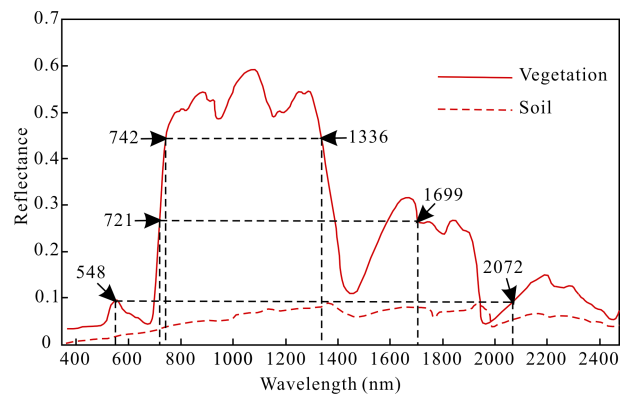


Fig. 5 Spectrum diagram of soil and vegetation. Three couples of spectral difference including 1699 nm and 721 nm, 1336 nm and 742 nm, and 2072 nm and 548 nm

Table 1 Principal components for six bands. Band1 is the difference between 2314 nm and 701 nm, Band2 is the difference between 1699 nm and 721 nm, Band3 is the difference between 1336 and 742 nm, Band4 is the difference between 2203 and 681 nm, Band5 is the difference between 2183 and 671 nm, Band6 is the difference between 2072 and 548 nm

Eigenvector	Band1	Band2	Band3	Band4	Band5	Band6
PC1	-0.4648	-0.1131	-0.2478	-0.2900	-0.3096	-0.7278
PC2	0.1082	0.7121	0.3305	0.2568	0.2415	-0.4974
PC3	-0.3725	0.6696	-0.2109	-0.3023	-0.2802	0.4453
PC4	0.7813	0.1602	-0.3988	-0.3786	-0.1932	-0.1549
PC5	-0.1495	0.0241	-0.44111	-0.2594	0.8455	-0.0144
PC6	0.0245	-0.0725	0.65665	-0.7401	0.1221	0.0149

4.4 Analysis of spatial geometric structure features

The scatter diagram of spectral image projects the pixel information of two or more bands onto a plane to analyze their distribution and clustering structure (Manolakis et al., 2003). This permits a large amount of data to be processed for its distribution and clustering independent of time. The scatter diagrams of two different remote sensing image's DN values have different graphic features that reflect change rules from a variety of ground objects. According to abnormal information delimited by the two-dimension scatter diagrams, their distribution should be available on the Hyperion image after pre-processing as similar objects dispersed in space should cluster together. Of interest, weak, alteration information was concentrated on the edge of the subject ellipse. The abnormal information was defined as Level 1 around its boundaries and Level 2 in the interior (Fig. 6), from which the average curves of abnormal information are calculated. The mean spectrum of every pixel in the red ellipse of the scatter plot (Fig. 6) was the test spectrum in Spectral Feature Fitting (SFF). When the matching degree of average curves was over 90%, the abnormal information was classified as the same type.

4.5 Spectral Feature Fitting (SFF)

SFF is used to match the spectra of images to the reference spectra from a field or spectral library. It tests specific absorption features after continuum removal for the reference spectra and the image (van der Meer, 2004). The absorption depth has the definition:

$$D = 1 - \frac{R_b}{R_c} \quad (2)$$

where D is the spectral absorption depth. R_b is the reflectance at the band bottom and R_c is the reflectance of the continuum at the same wavelength as R_b (Green and

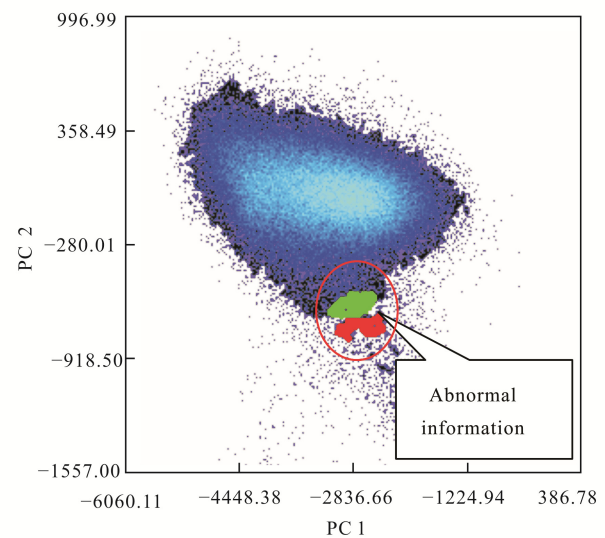


Fig. 6 Scatter diagram of PC1 and PC2. The green and red pixels in red ellipse are two different kinds of abnormal information

Craig, 1985). The degree to which the reference spectrum and the test spectrum match is expressed by the mean square error (RMS). The image spectrum matches well with the reference spectrum when the RMS value is small. An image of scale and RMS (scale/RMS) is generated for every reference spectrum. The scale/RMS image shows absorption characteristic depth, which is connected with material abundance. In the scale image, brighter pixels with low RMS errors demonstrate that they matched well with reference spectra. But if the incorrect reference end-members are entered or an incorrect wavelength range is applied, the result can be a large-scale value (> 1). Reference and image spectra are compared at each wavelength by least-squares and we can simultaneously calculate the RMS error for every reference spectrum and dark pixel on the RMS error image that represents low error. Locations that matched well with reference spectra are obtained by the scale image and RMS errors.

Reference spectra of alteration minerals were selected from the USGS spectral library. Test spectra were the mean spectrum of every pixel in the red ellipse of scattered plot. The reference spectra and test spectra needed a continuum removal process to enhance the spectral absorption features before SFF.

5 Results

Test spectra and reference spectra were matched by SFF to identify the abnormal minerals on the images. Pyrite, chlorite, calcite, dolomite, magnetite, hematite, sericite and muscovite were extracted from Hyperion data (Fig. 7). Verified sampling points were located in the area where altered minerals extracted. Sampling points were distributed in the area of mineral extraction with accessible transportation (Fig. 2). Rock samples were collected in the area where mineral concentrated as well as where

rock outcrops existed. To avoid human bias during rock sample collection, rocks that were dug out by tools in the natural outcrops and on the surface were collected at the same time. Rock samples were sliced in the laboratory and metallic minerals and nonmetallic minerals were identified under a high-resolution microscope. The comparison of identified results and extracted results for sample2, sample4, sample5, and sample8 are shown in Fig. 8–Fig. 11.

Ten validation samples were selected in the extracted mineral concentration area. Each point was found to contain magnetite, which indicates that the extraction of iron ore information was better in the images. A comparison of the extracted and identified results among the 10 samples indicated that the metallic minerals and non-metallic minerals extracted from seven verification points were consistent with the identified results (Table 2, Table 3).

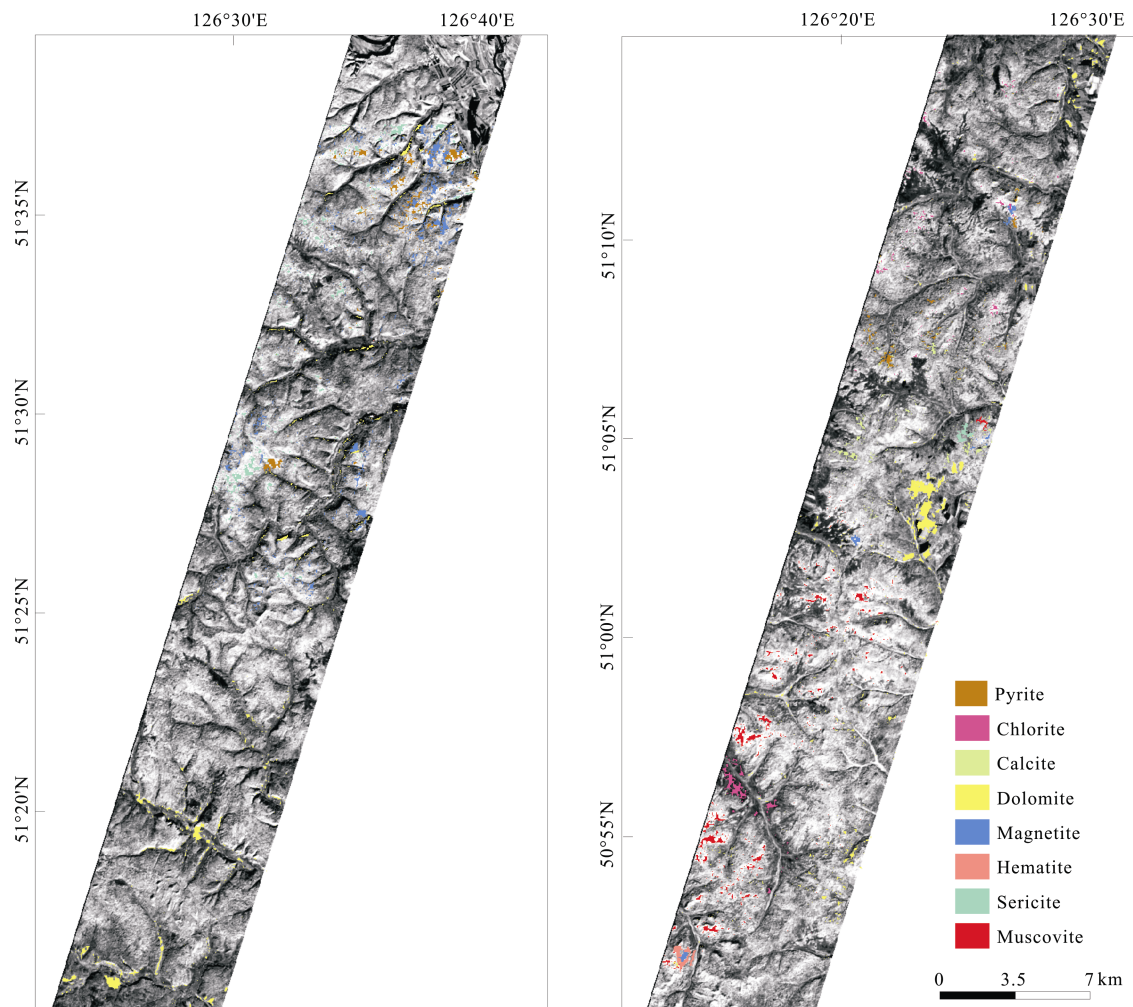


Fig. 7 Result of minerals extraction of Huma. SVSCD extraction result of pyrite (brownness), chlorite (ginger pink), calcite (green), dolomite (yellow), magnetite (blue), hematite (medium coral), sericite (cyan), and muscovite (red), overlain on Hyperion band 51

Table 2 The better comparison of mineral extraction results and identification results, the gray area is the verified sampling points

	Sample point	Metallic mineral	Nonmetallic mineral
Mineral extraction results	Sample 2	Pyrite, magnetite, hematite	Dolomite, sericite
	Sample 3	Pyrite, magnetite	Sericite, dolomite
	Sample 4	Pyrite, magnetite	Chlorite
	Sample 5	A little magnetite	Calcite, sericite, muscovite
	Sample 6	Siderite, magnetite	Muscovite
	Sample 8	Magnetite, a little pyrite	Sericite
	Sample 10	Magnetite, hematite	Muscovite, dolomite
Mineral identification results	Sample 2	Magnetite, pyrite, hematite	Iddingsitization olivine, clay minerals, amphibole
	Sample 3	Pyrite, magnetite	Partially particle sericitization , iddingsitization olivine, olivine
	Sample 4	Magnetite, pyrite,	Chlorite, actinolite, albite
	Sample 5	Magnetite	Sericitization staurolite, garnet, muscovite, quartz
	Sample 6	Magnetite	Muscovite, quartz, albite
	Sample 8	Magnetite	Carbonatation, sericitization feldspar
	Sample 10	Magnetite, hematite	Quartz, muscovite, biotite, feldspar particle sericitization

Table 3 The worse comparison of mineral extraction results and identification results

	Sample point	Metallic mineral	Nonmetallic mineral
Mineral extraction results	Sample 1	Magnetite	Dolomite
	Sample 7	Magnetite, pyrite	Sericite, dolomite
	Sample 9	Pyrite, magnetite, siderite	Sericite
Mineral identification results	Sample 1	Magnetite	Iddingsitization olivine
	Sample 7	Magnetite	Iddingsitization olivine, plagioclase partially particle sericitization
	Sample 9	Metallic mineral content at about 3%-5%, magnetite, pyrite	

The microscopic examination of sample 2 shows that detrital minerals are quartz and feldspar and that clay minerals have been transformed into crystalline biotite. Metallic minerals contain magnetite and 1% or less pyrite. The area of sample 2 contains clay minerals like dolomite, sericite with some properties of clay minerals, pyrite, magnetite and hematite. Clay minerals, magnetite, hematite and pyrite conform to the identification result (Fig. 8). The identified result of sample 4 contains chlorite, actinolite and albite. Metallic minerals magnetite and pyrite are approximately 1% of the sample. Chlorite, magnetite and pyrite are extracted from the sample 4 site according to the mineral map, which conforms to the identification results (Fig. 9). The identified result of rock sample 5 shows that nonmetallic mineral compositions including garnet, sericitization staurolite, muscovite and quartz. Metallic mineral (magnetite) content is about 1%–2%. The extracted results at the

sample 5 site contain magnetite, calcite, sericite and muscovite. The garnet and sericitization staurolite in the identified result are the products of muddy rocks that contain iron ions and aluminum ions transformed by regional metamorphism. This indicates that the region around sample 5 has abundant aluminum and iron minerals. Magnetite, sericite and muscovite in the extracted map conform to the laboratory identification (Fig. 10). The identified result of rock sample 8 under the microscope shows that mineral compositions including plagioclase and augite. The alteration is mainly carbonatation and feldspar sericitization. Magnetite content is about 2% and has a disseminated distribution. The mineral extracted result at sample 8 contains magnetite, some pyrite, sericite and dolomite (Fig. 11). Sericite and dolomite conform to the alteration of carbonatation and sericitization. Magnetite is also extracted at the sample 8 site.

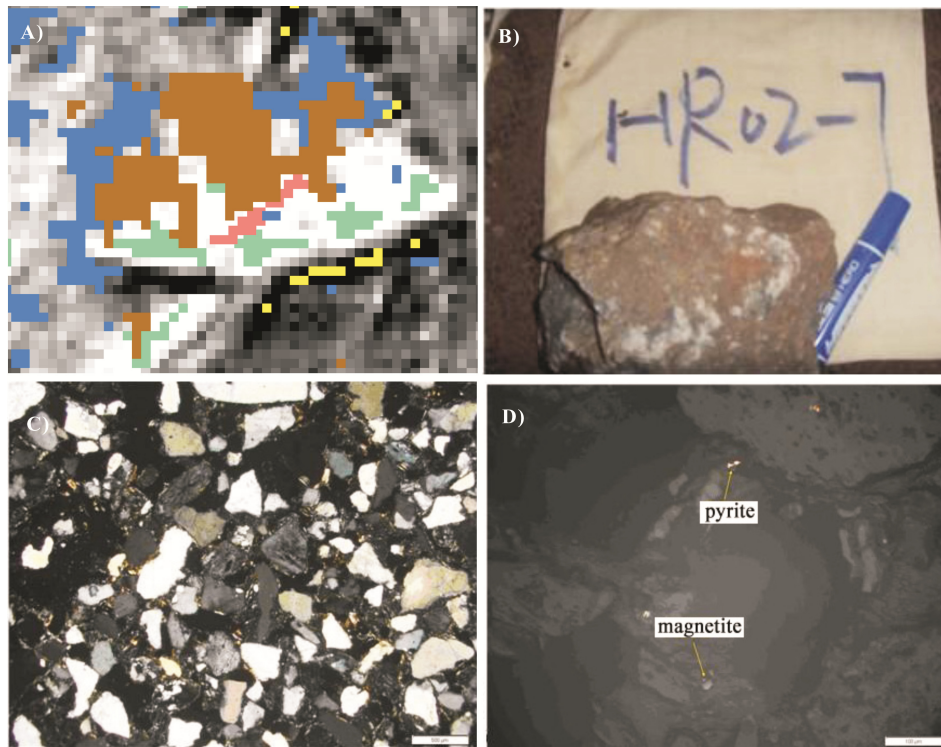


Fig. 8 The validation of sample 2: A) mineral extracted result of sample 2, including magnetite, hematite, pyrite, dolomite and sericite, B) rock sample, C) microscope photo: biotitization debris containing clay minerals, D) microscope photo: magnetite and pyrite

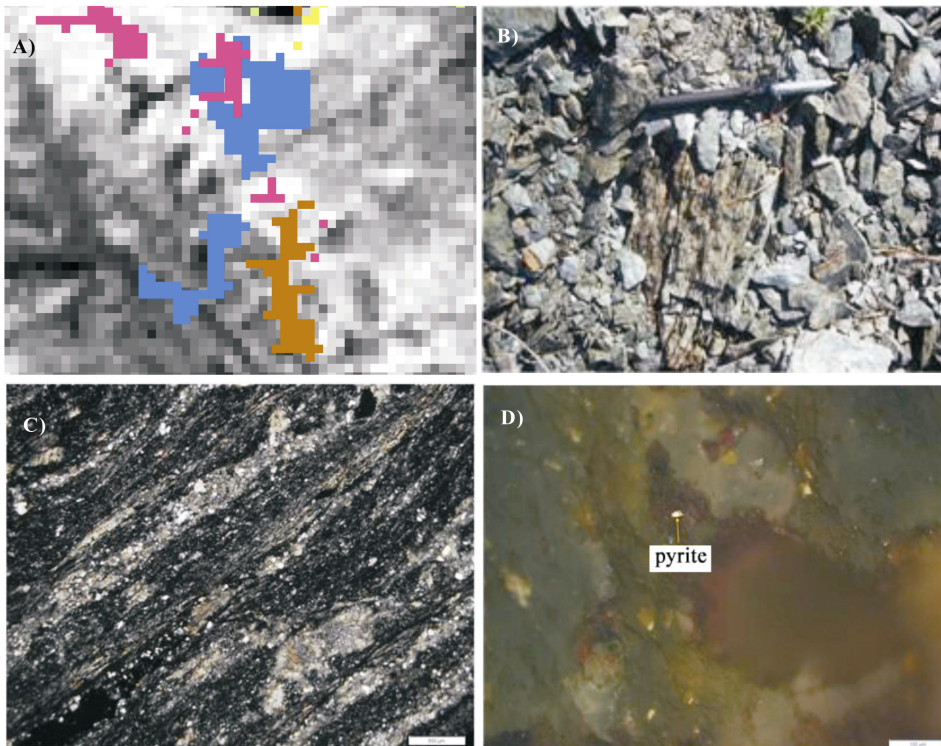


Fig. 9 The validation of sample 4: A) mineral extracted result of sample 4, including pyrite, magnetite and chlorite, B) rock sample, C) microscope photo: chlorite, D) microscope photo: pyrite

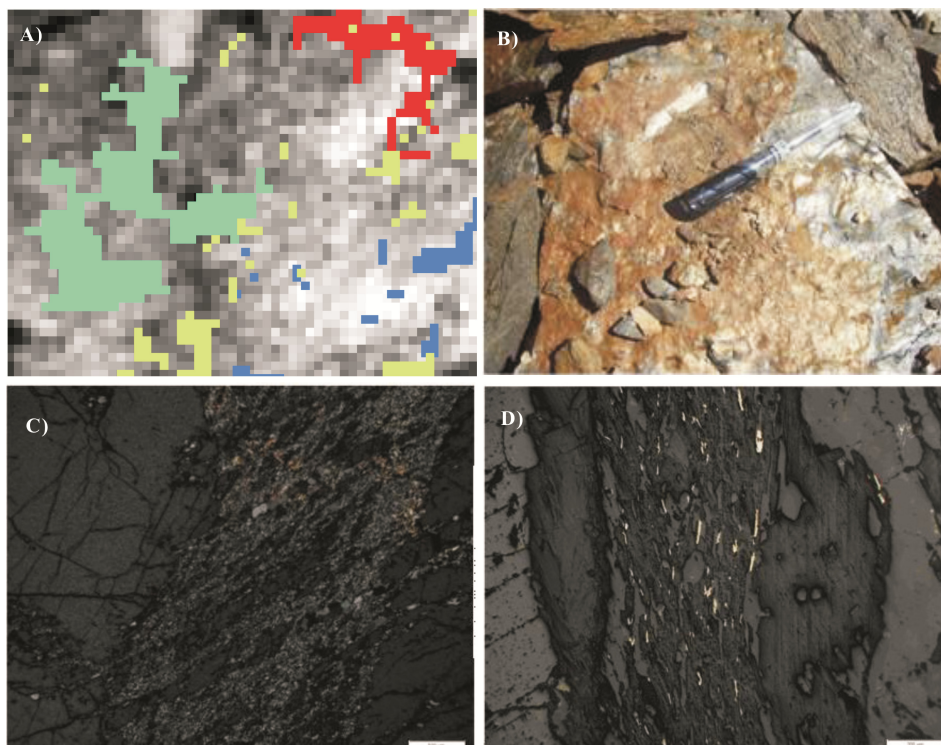


Fig. 10 The validation of sample 5: A) mineral extracted result of sample 5, including a little magnetite, calcite, sericite and muscovite, B) rock sample, C) microscope photo: muscovite, garnet, sericitization staurolite, D) microscope photo: magnetite

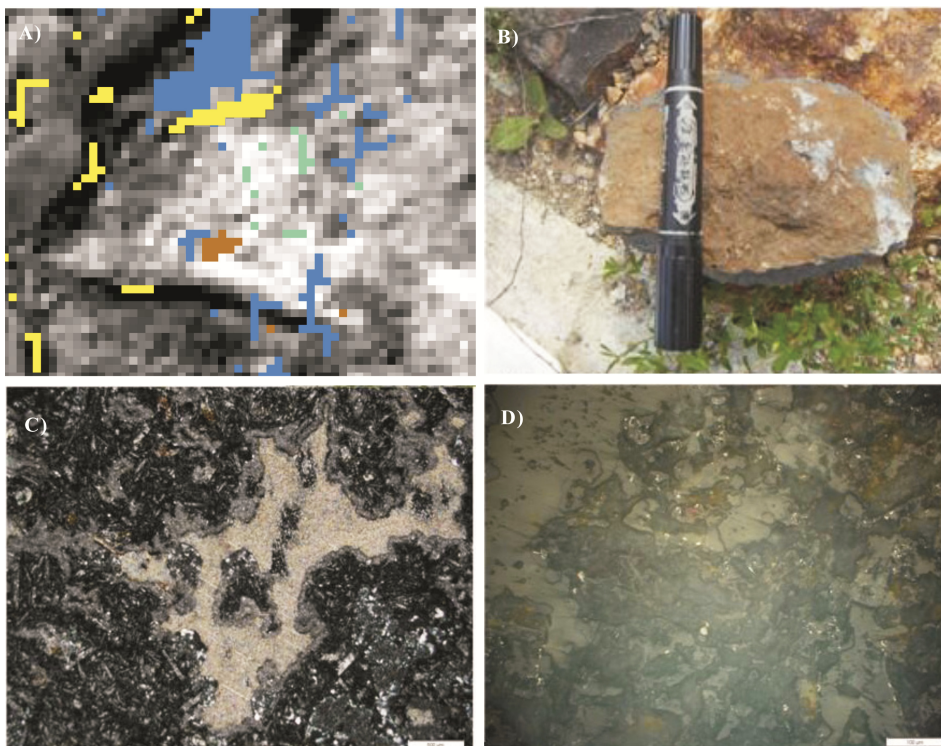


Fig. 11 The validation of sample 8: A) mineral extracted result of sample 5, including magnetite, some pyrite, sericite and dolomite, B) rock sample, C) microscope photo: carbonatation, feldspar sericitization, D) microscope photo: magnetite

6 Discussion

The scatter diagram of the wave band (after calculating the spectral difference) and the primitive wave band of images are shown in Fig. 12. Fig. 12A consists of band 192 and band 119 whose central wavelength is 2072 nm and 1336 nm. Contrasting Fig. 12A to Fig. 12B, shows that some information in the red ellipse has disappeared because band 192 is replaced with the spectral differences of 2072 nm and 548 nm. Fig. 12C is the scatter of two bands after applying a traditional vegetation suppression method from ENVI. After vegetation suppression and data preprocessing, Hyperion bands were rearranged. The band 192 with a center wavelength of 2072 nm changes to band 130, and band 119 changes to band 91. Fig. 12D is the scatter of two couples of spectral difference; one at 2072 nm and at 548 nm, the other is at 1336 nm and at 742 nm. Contrasting Fig. 12C to Fig.

12D, we also find that some information is inhibited because band 91 is replaced with pairs of spectral difference, 2072 and 548nm. Fig. 12C is similar to Fig. 12A. This shows that the ENVI vegetation suppression method is not effective. Fig. 13 shows that the correlation coefficient of the two plotted spectra is 0.9, indicating that SVSCD is an effective method to suppress vegetation information for mineral extracted in vegetation covered area.

7 Conclusions

SVSCD selected six pairs of bands centred at 2314 and 701 nm, 1699 and 721 nm, 1336 and 742 nm, 2203 and 681nm, 2183 and 671 nm, and 2072 and 548 nm, to detect altered minerals in vegetation covered areas. After band difference calculations from each data set, the vegetation information was suppressed and mineral

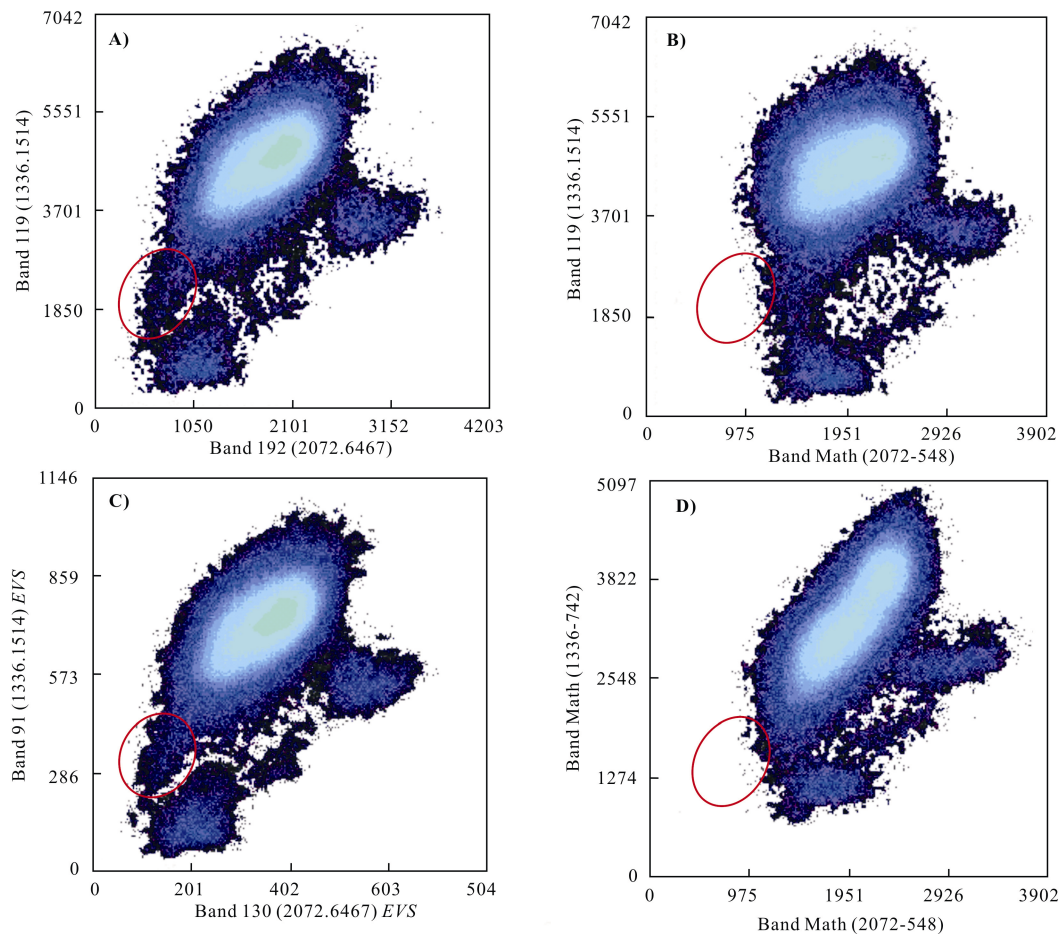


Fig. 12 Scatter plot of different band combination. A) Band 192 and band 119, B) spectral difference of 2072 nm and 548 nm and band 119, C) band 130 and band 91 (EVS is ENVI vegetation suppression method), D) two couples of spectral difference, one is 2072 nm and 548 nm, the other is 1336 nm and 742 nm

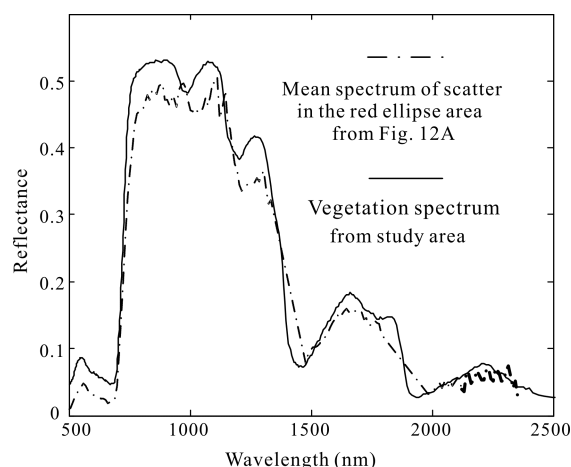


Fig. 13 Comparison of the suppressed information of Hyperion image and vegetation spectrum from study area

abnormal information was enhanced compared to the scatter plot of the original band. The spatial geometric structure features of PC1 and PC2 that have the largest difference of eigenvalues were used to identify the altered minerals by SFF.

Ten verified rocks samples from Huma study area of Heilongjiang Province were selected in the concentration of mineral extraction and analyzed under a high-resolution microscope to identify metal minerals and nonmetallic minerals. Results indicated that the extracted minerals, such as pyrite, magnetite, hematite, muscovite and chlorite, matched well with the component of verified samples, especially in sample 2, sample 4, sample 5 and sample 8.

The extracted minerals were consistent with identified minerals in sample 4 and sample 8, which indicated the extracted results of chloritization and sericitization alteration are better than others. Sericitization staurolite was found in sample 5. This is a product of muddy rocks that contain iron and aluminum ions transformed by regional metamorphism. The main metallic minerals in the study area were magnetite and pyrite. Mica containing aluminum ion was also distributed around sample 5. This was consistent with the formation conditions of sericitization staurolite. After analyzed extracted results and identified results comprehensively, the extracted results of iron oxides, muscovite, chlorite and sericitization alteration minerals matched well with identified results. All these demonstrated that SVSCD can effectively identify altered minerals in vegetation covered area in Hyperion images.

References

- Blouin C, Perry S, Lavell A et al., 2009. Reproducing the manual annotation of multiple sequence alignments using a SVM classifier. *Bioinformatics*, 25(23): 3093–3098. doi: 10.1093/bioinformatics/btp552
- Carranza E J M, Hale M, 2002. Mineral imaging with landsat thematic mapper data for hydrothermal alteration mapping in heavily vegetated terrane. *International Journal of Remote Sensing*, 23(2): 4827–4852. doi: 10.1080/01431160110115014
- Chen G Y, Qian S E, 2011. Denoising of hyperspectral imagery using principal component analysis and wavelet shrinkage. *IEEE Transactions on Geoscience and Remote Sensing*, 49(3): 973–980. doi: 10.1109/TGRS.2010.2075937
- Clark R N, 1999. Chapter 1: spectroscopy of rocks and minerals, and principles of spectroscopy. In: Rencz A N (ed). *Manual of Remote Sensing, Volume 3, Remote Sensing for the Earth Sciences*. New York: John Wiley and Sons, 3–58.
- Crowley J K, Hubbard B E, Mars J C, 2003. Analysis of potential debris flow source areas on Mount Shasta, California, by using airborne and satellite remote sensing data. *Remote Sensing of Environment*, 87(2–3): 345–358. doi: 10.1016/j.rse.2003.08.003
- Curran P J, Dungan J L, Peterson D L, 2001. Estimating the foliar biochemical concentration of leaves with reflectance spectrometry: testing the Kokaly and Clark methodologies. *Remote Sensing of Environment*, 76(3): 349–359. doi: 10.1016/S0034-4257(01)00182-1
- Di Tommaso I, Rubinstein N, 2007. Hydrothermal alteration mapping using ASTER data in the Infiernillo porphyry deposit, Argentina. *Ore Geology Reviews*, 32(1–2): 275–290. doi: 10.1016/j.oregeorev.2006.05.004
- Eklundh L, Singh A, 1993. A comparative analysis of standardised and unstandardised principal components analysis in remote sensing. *International Journal of Remote Sensing*, 14(7): 1359–1370. doi: 10.1080/01431169308953962
- El Desouky H A, Muchez P, Dewaele S et al., 2008. Postorogenic origin of the stratiform Cu mineralization at Lufukwe, Lufilian foreland, Democratic Republic of Congo. *Economic Geology*, 103(3): 555–582. doi: 10.2113/gsecongeo.103.3.555
- Gabr S, Ghulam A, Kusky T, 2010. Detecting areas of high-potential gold mineralization using ASTER data. *Ore Geology Reviews*, 38(1–2): 59–69. doi: 10.1016/j.oregeorev.2010.05.007
- Galvão L S, Almeida-Filho R, Vitorello Í, 2005. Spectral discrimination of hydrothermally altered materials using ASTER short-wave infrared bands: evaluation in a tropical savannah environment. *International Journal of Applied Earth Observation and Geoinformation*, 7(2): 107–114. doi: 10.1016/j.jag.2004.12.003
- Gong P, Pu R L, Biging G S et al., 2003. Estimation of forest leaf area index using vegetation indices derived from Hyperion hyperspectral data. *IEEE Transactions on Geoscience and Remote Sensing*, 41(6): 1355–1362. doi: 10.1109/TGRS.2003.

- 812910
- Green A A, Craig M D, 1985. Analysis of aircraft spectrometer data with logarithmic residuals. In: *Proceedings of the 3rd Airborne Imaging Spectrometer Data Analysis Workshop*. Pasadena, USA: JPL Publication, 111–119.
- Hu Bo, Zhu Guchang, Zhang Yuanfei et al., 2011. The application of spatial U-static method to the extraction of alteration anomalies. *Remote Sensing for Land & Resources*, (3): 71–76. (in Chinese)
- Hubbard B E, Crowley J K, Zimbelman D R, 2003. Comparative alteration mineral mapping using visible to shortwave infrared (0.4–2.4 μ m) Hyperion, ALI, and ASTER imagery. *IEEE Transactions on Geoscience and Remote Sensing*, 41(6): 1401–1410. doi: 10.1109/TGRS.2003.812906
- Hubbard B E, Crowley J K, 2005. Mineral mapping on the Chilean–Bolivian Altiplano using co-orbital ALI, ASTER and Hyperion imagery: data dimensionality issues and solutions. *Remote Sensing of Environment*, 99(1–2): 173–186. doi: 10.1016/j.rse.2005.04.027
- Hunt G R, 1977. Spectral signatures of particulate minerals in the visible and near infrared. *Geophysics*, 42(3): 501–513. doi: 10.1190/1.1440721
- Ju J C, Kolaczyk E D, Gopal S, 2003. Gaussian mixture discriminant analysis and sub-pixel land cover characterization in remote sensing. *Remote Sensing of Environment*, 84(4): 550–560. doi: 10.1016/S0034-4257(02)00172-4
- Landgrebe D, 2002. Hyperspectral image data analysis. *IEEE Signal Processing Magazine*, 19(1): 17–28. doi: 10.1109/79.974718
- Manolakis D, Marden D, Shaw G A, 2003. Hyperspectral image processing for automatic target detection applications. *Lincoln Laboratory Journal*, 14(1): 79–116.
- Massironi M, Bertoldi L, Calafa P et al., 2008. Interpretation and processing of ASTER data for geological mapping and granitoids detection in the Saghro massif (eastern Anti-Atlas, Morocco). *Geosphere*, 4(4): 736–759. doi: 10.1130/GES00161.1
- Mikucki E J, Ridley J R, 1993. The hydrothermal fluid of Archean lode-gold deposits at different metamorphic grades: compositional constraints from ore and wallrock alteration assemblages. *Mineralium Deposita*, 28(6): 469–481. doi: 10.1007/BF02431603
- Pour A B, Hashim M, 2011. Identification of hydrothermal alteration minerals for exploring of porphyry copper deposit using ASTER data, SE Iran. *Journal of Asian Earth Sciences*, 42(6): 1309–1323. doi: 10.1016/j.jseae.2011.07.017
- Pour A B, Hashim M, 2012a. The application of ASTER remote sensing data to porphyry copper and epithermal gold deposits. *Ore Geology Reviews*, 44: 1–9. doi: 10.1016/j.oregeorev.2011.09.009
- Pour A B, Hashim M, 2012b. Identifying areas of high economic-potential copper mineralization using ASTER data in the Urumieh-Dokhtar Volcanic Belt, Iran. *Advances in Space Research*, 49(4): 753–769. doi: 10.1016/j.asr.2011.11.028
- Pour A B, Hashim M, 2013. Fusing ASTER, ALI and Hyperion data for enhanced mineral mapping. *International Journal of Image and Data Fusion*, 4(2): 126–145. doi: 10.1080/19479832.2012.753115
- Pour A B, Hashim M, van Genderen J, 2013. Detection of hydrothermal alteration zones in a tropical region using satellite remote sensing data: Bau goldfield, Sarawak, Malaysia. *Ore Geology Reviews*, 54: 181–196. doi: 10.1016/j.oregeorev.2013.03.010
- Pour A B, Hashim M, Marghany M, 2014. Exploration of gold mineralization in a tropical region using Earth Observing-1 (EO1) and JERS-1 SAR data: a case study from Bau gold field, Sarawak, Malaysia. *Arabian Journal of Geosciences*, 7(6): 2393–2406. doi: 10.1007/s12517-013-0969-3
- Pour A B, Hashim M, 2014. ASTER, ALI and Hyperion sensors data for lithological mapping and ore minerals exploration. *SpringerPlus*, 3: 130. doi: 10.1186/2193-1801-3-130
- Rajendran S, Al-Khirbashi S, Pracejus B et al., 2012. ASTER detection of chromite bearing mineralized zones in Semail Ophiolite Massifs of the northern Oman Mountains: exploration strategy. *Ore Geology Reviews*, 44: 121–135. doi: 10.1016/j.oregeorev.2011.09.010
- Sabins F F, 1999. Remote sensing for mineral exploration. *Ore Geology Reviews*, 14(3–4): 157–183. doi: 10.1016/S0169-1368(99)00007-4
- Sillitoe R H, Hedenquist J W, 2003. *Volcanic, geothermal and ore-forming fluids: Rulers and witnesses of processes within the Earth: Linkages between volcanotectonic settings, ore-fluid compositions, and epithermal precious metal deposits*. Society of Economic Geologists and Geochemical Society Special Publications, 315–343.
- Sims D A, Gamon J A, 2003. Estimation of vegetation water content and photosynthetic tissue area from spectral reflectance: a comparison of indices based on liquid water and chlorophyll absorption features. *Remote Sensing of Environment*, 84(4): 526–537. doi: 10.1016/S0034-4257(02)00151-7
- Stoner E R, Baumgardner M F, 1981. Characteristic variations in reflectance of surface soils. *Soil Science Society of America*, 45(6): 1161–1165. doi: 10.2136/sssaj1981.03615995004500060031x
- van der Meer F, 2004. Analysis of spectral absorption features in hyperspectral imagery. *International Journal of Applied Earth Observation and Geoinformation*, 5(1): 55–68. doi: 10.1016/j.jag.2003.09.001
- Vaughan R G, Calvin W M, Taranik J V, 2003. Sebas hyperspectral thermal infrared data: surface emissivity measurement and mineral mapping. *Remote Sensing of Environment*, 85(1): 48–63. doi: 10.1016/S0034-4257(02)00186-4
- Vicente L E, de Souza Filho C R, 2011. Identification of mineral components in tropical soils using reflectance spectroscopy and advanced spaceborne thermal emission and reflection radiometer (ASTER) data. *Remote Sensing of Environment*, 115(8): 1824–1836. doi: 10.1016/j.rse.2011.02.023
- Wei Hao, Xu Jiuhua, Zeng Qingdong et al., 2011. Fluid evolution of alteration and mineralization at the Duobaoshan porphyry Cu (Mo) deposit, Heilongjiang Province. *Acta Petrologica Sinica*, 27(5): 1361–1374. (in Chinese)

- Yang J, Sun J, Ge Q et al., 2017. Assessing the impacts of urbanization-associated green space on urban land surface temperature: a case study of Dalian, China. *Urban Forestry & Urban Greening*. 22: 1–10. doi: 10.1016/j.ufug.2017.01.002.
- Yang Z A, Peng S L, Zhu G C et al., 2009. Spectrum spatial structure characteristic analysis of remote sensing alteration information and interference factors. *Journal of Central South University of Technology*, 16(4): 647–652. doi: 10.1007/s11771-009-0107-2
- Zhang Yuanfei, Yuan Jiming, Zhu Guchang et al., 2010. A study of spatial structure analysis and alteration information extraction based on random models of remote sensing data. *Remote Sensing for Land & Resources*, (4): 34–39. (in Chinese)